Full characterization of ultrathin 5-nm low-*k* dielectric bilayers: Influence of dopants and surfaces on the mechanical properties

Travis D. Frazer,[1,*] Joshua L. Knobloch,[1] Jorge N. Hernández-Charpak,[1] Kathleen M. Hoogeboom-Pot,[1] Damiano Nardi,[1] Sadegh Yazdi,[2] Weilun Chao,[3] Erik H. Anderson,[3] Marie K. Tripp,[4] Sean W. King,[4] Henry C. Kapteyn,[1] Margaret M. Murnane,[1] and Begoña Abad[1]

[1]*Department of Physics, JILA and STROBE NSF Science & Technology Center, University of Colorado and NIST, Boulder, Colorado 80309, USA*

[2]*Renewable and Sustainable Energy Institute, University of Colorado, Boulder, Colorado 80309, USA*

[3]*Center for X-Ray Optics, Lawrence Berkeley National Laboratory, Berkeley, California 94720, USA*

[4]*Intel Corp., 2501 NW 229th Ave., Hillsboro, Oregon 97124, USA*

(Received 6 May 2020; accepted 17 June 2020; published 13 July 2020)

Ultrathin films and multilayers, with controlled thickness down to single atomic layers, are critical for advanced technologies ranging from nanoelectronics to spintronics to quantum devices. However, for thicknesses less than 10 nm, surfaces and dopants contribute significantly to the film properties, which can differ dramatically from that of bulk materials. For amorphous films being developed as low dielectric constant interfaces for nanoelectronics, the presence of surfaces or dopants can soften films and degrade their mechanical performance. Here we use coherent short-wavelength light to fully and nondestructively characterize the mechanical properties of individual films as thin as 5 nm within a bilayer. In general, we find that the mechanical properties depend both on the amount of doping and the presence of surfaces. In very thin (5-nm) silicon carbide bilayers with low hydrogen doping, surface effects induce a substantial softening—by almost an order of magnitude—compared with the same doping in thicker (46-nm) bilayers. These findings are important for informed design of ultrathin films for a host of nano- and quantum technologies, and for improving the switching speed and efficiency of next-generation electronics.

DOI: 10.1103/PhysRevMaterials.4.073603

I. INTRODUCTION

Advanced nanoelectronics, spintronics, and quantum devices are becoming increasingly three dimensional in design, incorporating many layers of sub-10-nm ultrathin films. Moreover, these heterostructures must maintain optimal mechanical properties to avoid device failure. For example, softening due to high hydrogenation (doping with hydrogen) can lead to creep and delamination in semiconductor devices [1,2]. Additionally, as devices push to ever-smaller characteristic dimensions, the larger influence of surfaces and interfaces in nanoscale films can change the material properties compared to bulk materials. Depending on the composition of the film, nanoscale thickness effects have been shown to either soften or stiffen ultrathin films [3,4].

One mechanism for introducing a thickness dependence of the elastic properties of ultrathin films arises from the high proportion of atoms at the free surface of the material, which have a reduced number of nearest neighbors compared to atoms in the bulk volume. The low-coordinated surface can either soften the film since surface atoms have fewer constraints on their movement [5], or it can stiffen the film as redistributed electrons induce charging or bond contraction [6,7]. These mechanisms have been studied theoretically using continuum and atomistic approaches [5,7–11], and were measured experimentally in materials such as nitrides [12], semiconductors [10,13], polymers [14], and metals [15–17]. A second mechanism that can modify the elastic properties of ultrathin films is the influence of interfaces in multilayers [18]. For example, in few-nanometer-thick Ni/Ta bilayers, while their density ratio is not meaningfully changed from that expected in bulk, we have previously shown their elastic properties are significantly modified—nickel softens while tantalum stiffens, relative to their bulk counterparts [4]. However, in this past work we could not extract both of the two elastic constants that fully describe isotropic materials, which are critical to understanding dielectrics for nanoelectronics.

Dielectric thin films such as SiC:H and SiOC:H promise optimal electrical properties that are critical for continued scaling of computing power, but struggle to maintain good mechanical properties. To improve the efficiency and switching speed of the final device, the dielectric constant, k, of the material between the metallic circuit elements (the interlayer dielectric) needs to be low, below that of the silica used historically ($k = 4.2$) [1,19]. Methods to lower the dielectric constant include introducing more nonpolar bonds via hydrogenation, or introducing pores into the interlayer dielectric. However, the mechanical performance of the film degrades when the network of bonds in the bulk of the film becomes too disrupted, either by high levels of hydrogen bond termination [19–21] or porosity [22].

To measure the elastic properties of such thin films, it is very challenging for most techniques to probe <50-nm

*travis.frazer@colorado.edu

thicknesses. Widely used techniques such as nanoindentation can characterize films with thicknesses on the order of a fraction of a micron, when combined with advanced modeling [23,24]. Surface Brillouin light scattering, which uses the interaction of light and acoustic phonons, has extracted the full elastic tensor of films of thicknesses down to 25 nm [25]. However, it has difficulty characterizing thinner films without assuming one of the elastic constants. In past work, we used coherent extreme ultraviolet (EUV) beams to characterize the full elastic tensor of isotropic ultrathin films down to 11 nm in thickness [21]. This allowed us to simultaneously extract the Young modulus and Poisson's ratio of low-k amorphous SiC:H films with varying degrees of stiffness and hydrogenation, in a single measurement.

In this work, we show how dopants and surfaces interplay to determine the elastic properties of low-k ($k < 4.2$) dielectric films that are being developed for next-generation nanoelectronics. We use coherent short-wavelength light to fully and nondestructively characterize the mechanical properties of SiOC:H films and SiC:H bilayers with individual layers as thin as 5 nm. This allows us to distinguish between dopant-induced and surface-induced softening. For example, in very thin (5-nm) silicon carbide films with low hydrogen doping, surface effects induce a substantial softening—by almost an order of magnitude—compared with the same doping in thicker (46-nm) films. These findings are important for informed design of ultrathin films for a host of nano- and quantum technologies, and for improving the switching speed and efficiency of next-generation electronics.

II. METHODS

To distinguish between surface-induced softening and dopant-induced softening, we compare two different sample materials: high-hydrogenation amorphous SiC:H and low-hydrogenation amorphous SiOC:H. Each sample is fabricated by plasma-enhanced chemical vapor deposition from diluted organosilane precursors on 300-mm-diameter Si (001) by Intel Corp., as described in Refs. [19,26,27]. To describe the number of atomic bonds broken by hydrogenation in each material, we use nominal values of network connectivity (or average atomic coordination number), as determined by Rutherford backscattering and nuclear reaction analysis [28] at Intel Corp. See Supplemental Material for the nominal film properties, including k [29]. As described by topological constraint theory [30,31], an amorphous material transitions from flexible to rigid when the number of constraints on each atom, n, equals the number of degrees of freedom. Accounting for the fixed bond lengths and the fixed bond angles, the relation between network connectivity, $\langle r \rangle$, and constraints, n, is $n = \langle r \rangle/2 + (2\langle r \rangle - 3)$. To constrain all three degrees of freedom, $\langle r \rangle$ has a critical value at 2.4, known as the rigidity percolation threshold, where the coordination is high enough for a rigid network of bonds to percolate through the film volume. Our SiC:H samples have $\langle r \rangle = 3.2$, and thus are rigid, while our SiOC:H samples have been hydrogenated to the critical value of 2.4, which makes films softer and less compressible, as we have previously shown [21]. By characterizing the elastic properties of several thicknesses of both materials, we investigate surface-induced softening both above and below the critical level of hydrogen doping.

We characterize the elastic properties of ultrathin films using the EUV nanometrology technique described in Refs. [4,21,32]. First, we deposit an array of Ni nanoline grating transducers on each sample using e-beam lithography and liftoff. Grating periods range from 1.5 μm to 40 nm, as characterized by atomic force microscopy [29,33]. We laser excite these transducers using an ultrafast (30-fs), near-infrared (780-nm) pump pulse, as illustrated in Fig. 1(a). The resulting impulsive thermal expansion of the nanolines launches acoustic waves in the nanolines and the film. At early times, a longitudinal acoustic wave propagates down into the sample and reflects from any buried interfaces back to the surface [Fig. 1(b)]. On longer timescales, a surface acoustic wave dominates, with a wavelength defined by the grating period [Fig. 1(c)]. The longitudinal breathing mode of the nanolines is also excited, which we have previously used to characterize the nanolines' elastic properties [4] [Fig. 1(c)].

We measure these dynamic surface deformations by diffracting a time-delayed, ultrafast (10-fs) coherent EUV probe pulse from the surface. The probe has 29-nm wavelength (43-eV photon energy), obtained via high-harmonic generation [34]. This photon energy is far from any absorption edges in our sample materials, ensuring minimal sensitivity to hot electrons, which can dominate visible-wavelength measurements at the few-picosecond timescales of interest to this work [e.g., Fig. 1(b)]. Our EUV probe provides a direct and sensitive (∼pm sensitivity) [35] measurement of the surface acoustic waves and longitudinal acoustic waves in the film. By fitting the acoustic wave velocities using a finite-element analysis (FEA) procedure [21,36–38], we extract the two independent components of the isotropic elastic tensor of the film: c_{11} and c_{44}, or equivalently Young's modulus and Poisson's ratio (see Supplemental Material) [29,39].

III. RESULTS AND DISCUSSION

Our samples are deposited in two geometries: the SiC:H samples are bilayers (a stack of two identical layers on a Si substrate, see Fig. 2), and the SiOC:H samples are films (a single film on a Si substrate). The two SiC:H bilayer samples compare two different layer thicknesses, 46 and 5 nm, and we extract the elastic properties of the topmost layer to check for softening due to the free surface. The SiOC:H films compare three different thicknesses, 44, 19, and 11 nm, and have higher hydrogenation than the SiC:H bilayers, as already described. Most importantly, all of the samples we measure are nonporous. This isolates the influence of the single free surface at the top of the film stack. Porous SiOC:H has been shown to have constant elastic properties down to 25-nm thickness [22], but the pores create multiple surfaces throughout the volume of the film, complicating a comparison between surface-induced softening and doping-induced softening in that case.

To extract the mechanical properties of the ultrathin films, our model requires *a priori* thicknesses and densities for each film. X-ray reflectivity provides these values for the SiOC:H films [29], but it is unable to distinguish the individ-

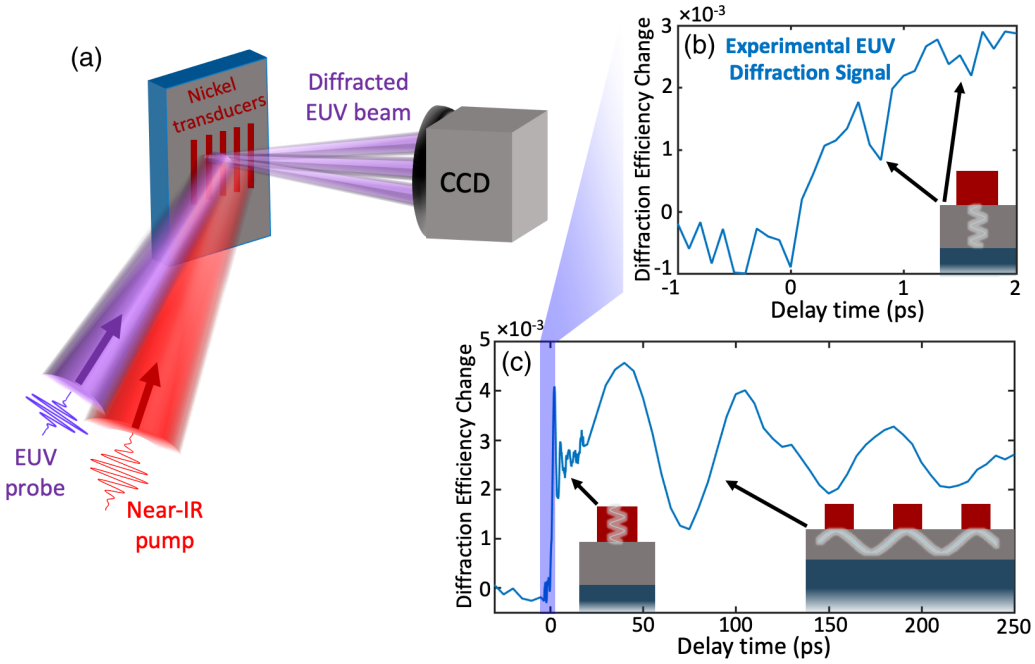

FIG. 1. Dynamic EUV diffraction from transverse and longitudinal acoustic waves. (a) After ultrafast laser excitation, the hot Ni nanolines impulsively expand, launching acoustic waves in the sample. After a controlled time delay, an EUV probe pulse diffracts from the sample surface, and the scattered light is collected by a charge-coupled device camera. The acoustic waves dynamically change the EUV diffraction efficiency, as shown in (b) and (c). (b) A longitudinal acoustic wave is launched downward into the film (inset). Reflections from the film-substrate interface imprint a discrete series of echoes in the data (see arrows in inset). (c) At early times, we observe the longitudinal breathing mode (left) of the nanolines. At longer times, we observe a surface acoustic wave (right), whose penetration depth is confined to a fraction of the grating period. The surface acoustic wave and longitudinal acoustic wave velocities provide the two independent components of the isotropic film's elastic tensor.

ual layer thicknesses in the SiC:H bilayers. For the bilayers, we instead utilize scanning transmission electron microscopy (STEM) and energy-dispersive x-ray spectroscopy (EDS) to validate the precise thicknesses and compositions of all the layers we expect in the bilayer samples, as shown in Fig. 2. During sample fabrication, a nitrogen plasma treatment was performed before each SiC:H layer deposition, creating two additional 2-nm N-rich layers [Fig. 2(b)]. Moreover, as STEM was performed after the EUV measurements, we also observe a layer of amorphous carbon on top of the sample, which both the electron and the EUV beams can deposit during the measurement [40]. We also observe strain-induced contrast in both the Si substrate and the lower SiC:H layer, which will be discussed below.

To enhance the EUV measurement sensitivity to the influence of a free surface on the elastic properties of the film, we confine the acoustic waves predominantly into the top SiC:H layer. We do this by launching surface acoustic waves

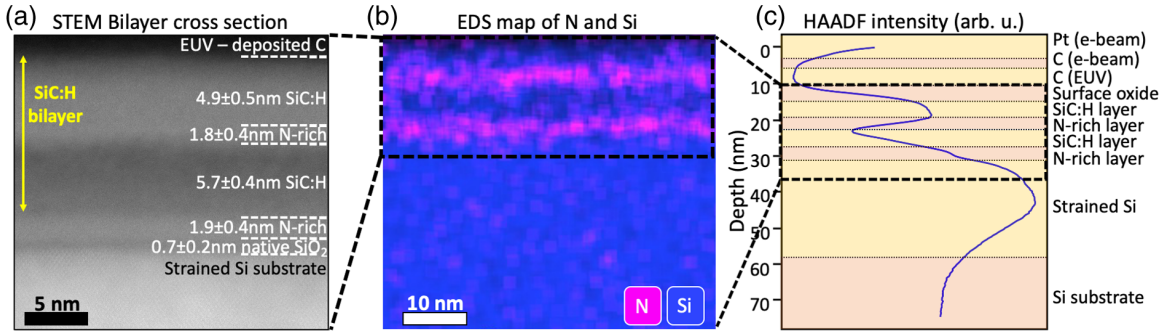

FIG. 2. Compositional characterization of the 5-nm SiC:H bilayer. (a) STEM image obtained using a HAADF detector. Strain from the deposited films blurs the atomic contrast peaks in the Si substrate, as expected [41]. HAADF intensity also drops at the interface of the two films in the bilayer. We attribute this to a reduction in the density of the bottom SiC:H layer, as it is strained by the layers above it. (b) EDS image of the sample showing Si (blue) and N (pink). Nitrogen exists at the bottom interfaces of the two SiC:H layers due to the nitrogen plasma clean applied to improve the film adhesion. (c) Horizontally binned lineout of the HAADF contrast for the full cross section taken for STEM characterization. This lineout extends upwards into the focused ion beam (FIB)-deposited Pt layer used for STEM, and downwards into the strained region of the Si substrate.

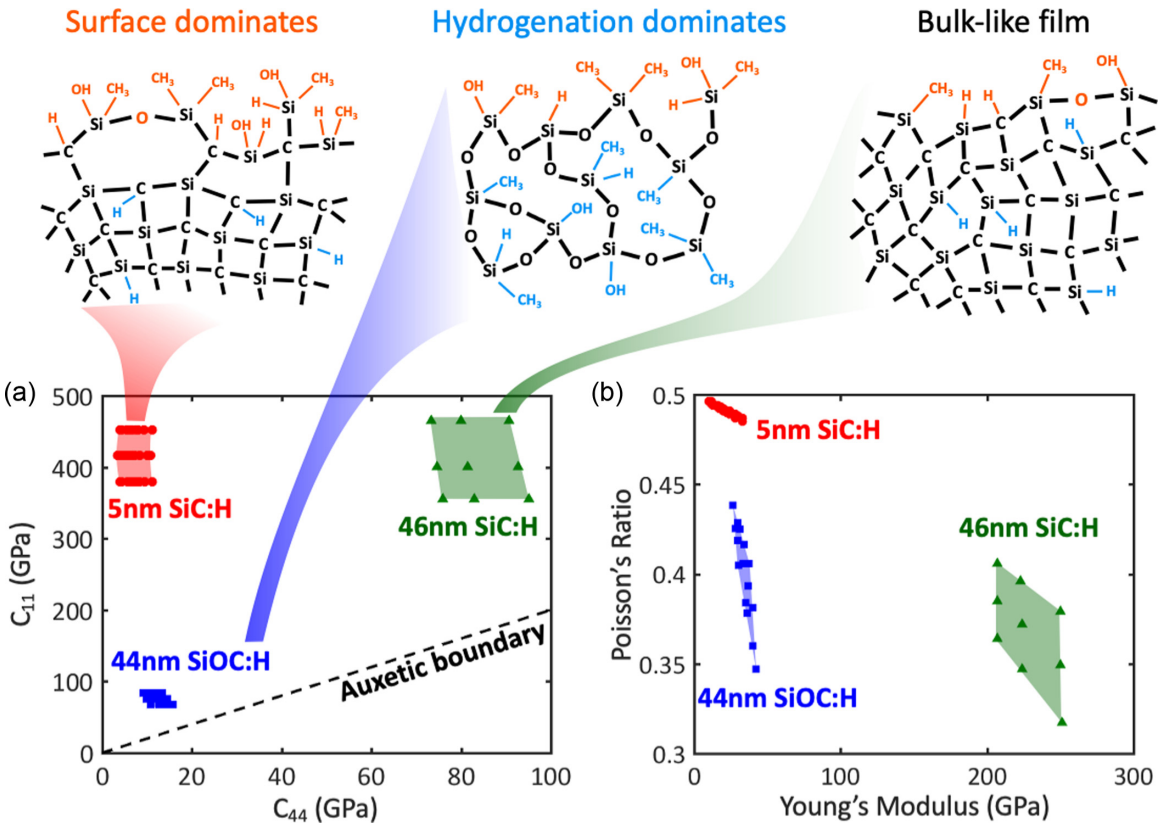

FIG. 3. Surface-induced softening compared to hydrogenation-induced softening. (a) Elastic constant ranges for the 5-nm SiC:H top layer (red circles), the 46-nm SiC:H top layer (green triangles), and the highly hydrogenated 44-nm SiOC:H film (blue squares). Each point represents a configuration simulated in the FEA model that agrees with the data, within uncertainty. The 46-nm film maintains a bulklike rigid bond network, due to its low hydrogenation and large thickness. The 5-nm film of the same material is significantly softened due to the terminated bonds at its surface (orange). This is distinct from the softening observed in highly hydrogenated SiOC:H, where hydrogenation breaks up the rigid bond network in the volume of the film (blue). Note the top schematics are to illustrate the differences between samples, and are not exact. The auxetic boundary, defined by $c_{11} = 2c_{44}$, is the limit where Poisson's ratio becomes negative. (b) The same data as in (a), expressed in terms of Poisson's ratio and Young's modulus.

with a 40-nm-period grating, which sets their wavelength and confines their penetration depth to $\sim 1/\pi$ of this period [36,37,42]. With most of the elastic energy confined to the topmost layer, we are able to reliably fit the elastic properties without any contribution from spurious effects from the lower layers. We account for the effects of the EUV deposited carbon, N-rich layers, and strain in our FEA model, as described in the Supplemental Material [29,43–45].

As shown in Fig. 3, we observe a strong softening in the low-hydrogenation SiC:H top layer when the thickness is reduced from 46 to 5 nm. This is mainly due to a reduced value of c_{44}, while c_{11} stays approximately constant [Fig. 3(a)]. In terms of Young's modulus and Poisson's ratio [Fig. 3(b)], the 5-nm SiC:H layer has a lower Young's modulus but higher Poisson's ratio, i.e., it is softer and more incompressible, like a polymer film. Note that the range of allowed elastic properties defines a nonsquare region (shaded in Fig. 3), after propagating the symmetric experimental uncertainty though the analysis process (see Supplemental Material [29]). While the 46-nm top layer maintains a bulklike rigid bond network, due to its low hydrogenation and large thickness, the 5-nm top layer of the same material is significantly softened due to the terminated bonds at its surface (orange in Fig. 3). This behavior is distinct from the softening observed in highly hydrogenated SiOC:H, where hydrogenation breaks up the rigid bond network in the volume of the film (blue in Fig. 3). This measurement of the 5-nm SiC:H layer represents the full characterization of a < 10 nm film without assuming any of the elastic constants.

The results on high-hydrogenation SiOC:H contrast with the results on low-hydrogenation SiC:H. First, the SiOC:H films have been hydrogenated past the critical number of broken bonds, meaning that the thickest, 44-nm film is expected to have lower c_{11} and c_{44} values than the SiC:H samples [Fig. 3(a)]. This places the region of allowed elastic constants close to the auxetic boundary, defined by $c_{11} = 2c_{44}$, below which Poisson's ratio becomes negative. This appears as a larger distortion after converting to Young's modulus and Poisson's ratio [Fig. 3(b)]. Comparing different SiOC:H film thicknesses, there is no discernible change in elastic properties since the regions of allowed elastic properties overlap for all three film thicknesses, with the only difference being an increased experimental uncertainty for the thinner films. For clarity, only the thickest SiOC:H film is shown in Fig. 3, but all three films' results are shown in the Supplemental Material [29].

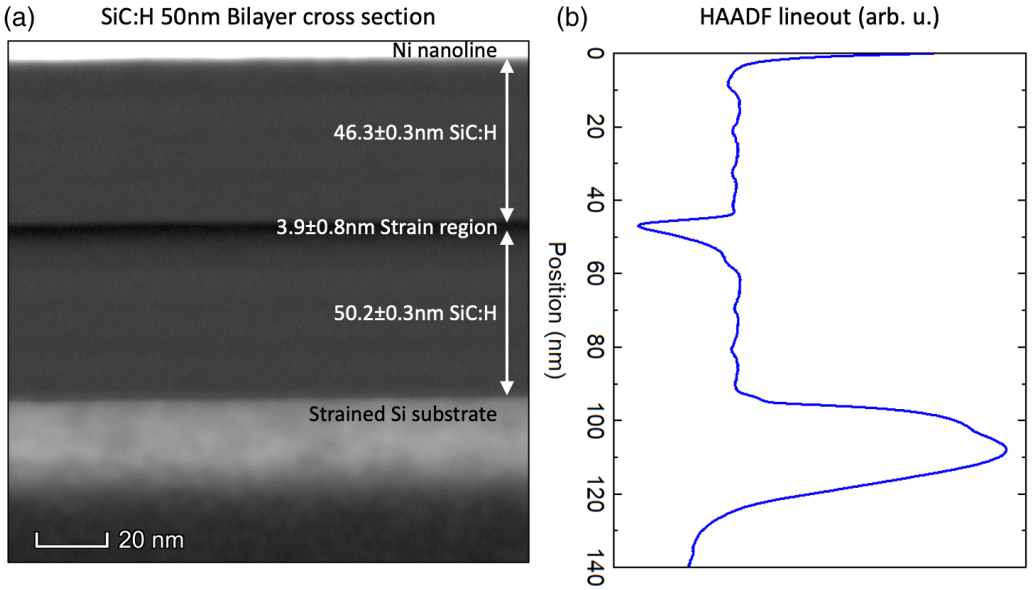

FIG. 4. STEM cross section of 46-nm SiC:H bilayer. (a) Full HAADF image. SiC:H films are known to strain Si substrates, and the full depth of the strained volume is visible here in the blurring of the atomic peaks imaged in the substrate region. We attribute the low-intensity region between the two SiC:H layers to a reduction in density as the top layer and N-rich layer similarly strain the bottom layer. Note the thickness of this strained region is similar to the layer thickness for the 5-nm bilayer in Fig. 2(a), indicating the same effect is lowering the HAADF intensity in the bottom layer of both SiC:H samples. (b) Lineout by horizontally binning (a). The faint intensity striations within each SiC:H layer are a result of the four-step deposition process. Each step is identical, with no change in film composition.

From the results presented above, we observe no surface-induced softening in highly hydrogenated SiOC:H, but we observe a significant surface-induced softening in lowly hydrogenated SiC:H. Our measurements indicate that this behavior comes from a competition between bond termination at the free surface, and bond termination in the bulk of the film due to hydrogenation. Both of these mechanisms reduce the rigid constraints on atoms, but only so many bonds can be terminated before a critical threshold is passed and the material loses its rigidity. As described above, the SiOC:H films have surpassed this critical threshold due to hydrogenation alone. Thus, the free surface can only have a minimal effect as the film thickness is reduced. The SiC:H bilayers, however, have less hydrogenation, well below the critical threshold. This allows the top layer to have a greater difference between the rigid bond network in its volume, and the terminated bonds at its free surface. When the layer thickness is reduced, the free surface can then begin to dominate over the otherwise rigid volume of SiC:H, softening the entire top layer. Importantly, the softening we observe in the 5-nm bilayer is not due to oxidation making the SiC:H equivalent to the SiOC:H films. X-ray photoelectron spectroscopy has shown SiC:H to be highly oxidation resistant [46,47], so any oxygen content in the SiC:H bilayer is much lower than in the SiOC:H films and likely is confined only to the outermost atomic layer, as indicated in Fig. 3 and corroborated by EDS (see Supplemental Material) [29]. Moreover, oxygen is twofold coordinated, so its presence still has the net effect of reducing the surface bond coordination.

To confirm the interpretation of our results as a surface softening effect, we perform further STEM and EDS characterizations of the thicker SiC:H bilayer to verify that it is identical in composition to the thinner bilayer. In the STEM cross section of the 46-nm bilayer (see Fig. 4), we observe similar changes in layer contrast as in the 5-nm bilayer. Specifically, we observe a region of reduced high-angle annular dark-field (HAADF) intensity at the top of the lower layer (just below the N-rich layer). Because the SiC:H layers are thicker for this sample, we can see here that the reduced intensity has a finite penetration depth of about 4 nm into the lower layer. This depth is comparable to the layer thickness of the thinner bilayer sample, and so we attribute the intensity reduction in both samples to the top layer straining the bottom layer. We similarly observe a clear strain layer in the Si substrate due to the lower SiC:H layer, as expected for such films on Si [41]. For the EDS measurements, there is no direct sensitivity to hydrogen, but they provide a self-consistent evaluation of the relative amounts of Si, C, O, and N through the depth of each bilayer sample. For both the top and bottom SiC:H layers of both the 5- and 46-nm bilayers, we measure consistent values of $\sim$85% Si, $\sim$12% C, and $<$2% each of O and N, which is within the noise floor. See the Supplemental Material for full EDS maps of each bilayer [29]. These characterizations together confirm there is no large discrepancy in fabrication between the two bilayer samples, and the primary difference between them is layer thickness.

Finally, we rule out alternative explanations for the change in elastic properties between the two SiC:H bilayers. First, a large strain reducing the density of the lower layer cannot explain our results. Reduced density would systematically shift our results toward higher elastic constants (an opposite trend to our observations)—moreover, our fitting procedure is largely insensitive to the density of the lower layer. Second, our observations cannot be explained by the nitrogen plasma treatment. If the treatment was causing a change in the elastic properties of lower layers, then the effect should be even more

pronounced when studying a multilayer SiC:H stack with a plasma treatment on each layer. In Ref. [26], the authors perform nanoindentation on exactly this case, with identical SiC:H layers as in our samples. They observe no significant difference in the average elastic properties of the multilayers, both with and without the plasma treatment, down to a layer thickness of 2.6 nm. This indicates buried N-rich layers do not change the overall elastic properties of a stack of SiC:H films. Our technique, however, enables us to isolate only the top layer of our bilayer samples, where the free surface dominates, independent of any plasma treatment on the lower layer. Lastly, we cannot fit our data with nominal SiC:H layer properties while only varying the elastic constants of the N-rich interface layers.

IV. CONCLUSION

We use coherent EUV beams to fully characterize the mechanical properties of films as thin as 5 nm. We find that in the top 5-nm layer of a SiC:H bilayer, surface effects induce a substantial softening—by almost an order of magnitude—compared with thicker, 46-nm SiC:H bilayers. This contrasts with SiOC:H films at high hydrogenation levels, which have no significant surface-induced softening, down to 11 nm. We attribute this difference between the two sample sets to the competing effects of terminated bonds in the volume of the film due to hydrogenation, and the terminated bonds defining the free surface of the film. For the free surface to change film elastic properties, the surface atoms must be undercoordinated compared to the atoms in the volume of the film. Once hydrogenation terminates enough bonds in the bulk of the film, atoms in the volume and surface of the film no longer have significantly different coordination numbers, and no thickness dependence is observed. These findings are important for informed design of ultrathin, robust films for a host of nano- and quantum technologies, and particularly for improving the switching speed and efficiency of next-generation electronics.

ACKNOWLEDGMENTS

The authors gratefully acknowledge support from the STROBE National Science Foundation Science & Technology Center, Grant No. DMR-1548924 and a Gordon and Betty Moore Foundation EPiQS Award through Grant No. GBMF4538. J.L.K. acknowledges support from an SRC Fellowship. H.C.K. is partially employed by KMLabs. W.C. gratefully acknowledges support through the US Department of Energy under Contract No. DE-AC02-05CH11231.

[1] D. Shamiryan, T. Abell, F. Iacopi, and K.Maex, Low-k dielectric materials, Mater. Today **7**, 34 (2004).

[2] A. Grill, S. M. Gates, T. E. Ryan, S. V. Nguyen, and D. Priyadarshini, Progress in the development and understanding of advanced low k and ultralow k dielectrics for very large-scale integrated interconnects—state of the art, Appl. Phys. Rev. **1**, 011306 (2014).

[3] L. G. Zhou and H. Huang, Are surfaces elastically softer or stiffer? Appl. Phys. Lett. **84**, 1940 (2004).

[4] K. M. Hoogeboom-Pot, E. Turgut, J. N. Hernandez-Charpak, J. M. Shaw, H. C. Kapteyn, M. M. Murnane, and D. Nardi, Nondestructive measurement of the evolution of layer-specific mechanical properties in sub-10 nm bilayer films, Nano Lett. **16**, 4773 (2016).

[5] R. J. Wang, C. Y. Wang, and Y. T. Feng, Effective geometric size and bond-loss effect in nanoelasticity of GaN nanowires, Int. J. Mech. Sci. **130**, 267 (2017).

[6] C. Q. Sun, Size dependence of nanostructures: Impact of bond order deficiency, Prog. Solid State Chem. **35**, 1 (2007).

[7] C. A. Yuan, O. van der Sluis, G. Q. Zhang, L. J. Ernst, W. D. van Driel, R. B. R. van Silfhout, and B. J. Thijsse, Chemical–mechanical relationship of amorphous/porous low-dielectric film materials. Comput. Mater. Sci. **42**, 606 (2008).

[8] R. E. Miller and V. B. Shenoy, Size-dependent elastic properties of nanosized structural elements, Nanotechnology **11**, 139 (2000).

[9] R. Dingreville, J. Qu, and M. Cherkaoui, Surface free energy and its effect on the elastic behavior of nano-sized particles, wires and films, J. Mech. Phys. Solids **53**, 1827 (2005).

[10] A. I. Fedorchenko, A.-B. Wang, and H. H. Cheng, Thickness dependence of nanofilm elastic modulus, Appl. Phys. Lett. **94**, 152111 (2009).

[11] B. Gong, Q. Chen, and D. Wang, Molecular dynamics study on size-dependent elastic properties of silicon nanoplates. Mater. Lett. **67**, 165 (2012).

[12] D. C. Hurley, V. K. Tewary, and A. J. Richards, Thin-film elastic-property measurements with laser-ultrasonic SAW spectrometry, Thin Solid Films **398–399**, 326 (2001).

[13] X. Li, T. Ono, Y. Wang, and M. Esashi, Ultrathin single-crystalline-silicon cantilever resonators: Fabrication technology and significant specimen size effect on young's modulus, Appl. Phys. Lett. **83**, 3081 (2003).

[14] C. M. Stafford, B. D. Vogt, C. Harrison, D. Julthongpiput, and R. Huang, Elastic moduli of ultrathin amorphous polymer films, Macromolecules **39**, 5095 (2006).

[15] P.-O. Renault, E. Le Bourhis, P. Villain, Ph. Goudeau, K. F. Badawi, and D. Faurie, Measurement of the elastic constants of textured anisotropic thin films from x-ray diffraction data, Appl. Phys. Lett. **83**, 473 (2003).

[16] H. Ogi, M. Fujii, N. Nakamura, T. Shagawa, and M. Hirao, Resonance acoustic-phonon spectroscopy for studying elasticity of ultrathin films, Appl. Phys. Lett. **90**, 191906 (2007).

[17] H. Ogi, M. Fujii, N. Nakamura, T. Yasui, and M. Hirao, Stiffened Ultrathin Pt Films Confirmed by Acoustic-Phonon Resonances, Phys. Rev. Lett. **98**, 195503 (2007).

[18] N. Nakamura, H. Ogi, T. Yasui, M. Fujii, and M. Hirao, Mechanism of Elastic Softening Behavior in a Superlattice, Phys. Rev. Lett. **99**, 035502 (2007).

[19] S. W. King, J. Bielefeld, G. Xu, W. A. Lanford, Y. Matsuda, R. H. Dauskardt, N. Kim, D. Hondongwa, L. Olasov, B. Daly, G. Stan, M. Liu, D. Dutta, and D. Gidley, Influence of network bond percolation on the thermal, mechanical, electrical and optical properties of high and low-k a-SiC:H thin films, J. Non-Cryst. Solids **379**, 67 (2013).

[20] H. Li, J. M. Knaup, E. Kaxiras, and J. J. Vlassak, Stiffening of organosilicate glasses by organic cross-linking, Acta Mater. **59**, 44 (2011).

[21] J. N. Hernandez-Charpak, K. M. Hoogeboom-Pot, Q. Li, T. D. Frazer, J. L. Knobloch, M. Tripp, S. W. King, E. H. Anderson, W. Chao, M. M. Murnane, H. C. Kapteyn, and D. Nardi, Full characterization of the mechanical properties of 11–50 Nm ultrathin films: Influence of network connectivity on the poisson's ratio, Nano Lett. **17**, 2178 (2017).

[22] J. Zizka, S. King, A. Every, and R. Sooryakumar, Acoustic phonons and mechanical properties of ultra-thin porous low-k films: A surface brillouin scattering study, J. Electron. Mater. **47**, 3942 (2018).

[23] K. Geng, F. Yang, and E. A. Grulke, Nanoindentation of submicron polymeric coating systems, Mater. Sci. Eng. A **479**, 157 (2008).

[24] J. Hay and B. Crawford, Measuring substrate-independent modulus of thin films, J. Mater. Res. **26**, 727 (2011).

[25] J. Zizka, S. King, A. G. Every, and R. Sooryakumar, Mechanical properties of low- and high-k dielectric thin films: A surface brillouin light scattering study. J. Appl. Phys. **119**, 144102 (2016).

[26] A. Giri, S. W. King, W. A. Lanford, A. B. Mei, D. Merrill, L. Li, R. Oviedo, J. Richards, D. H. Olson, J. L. Braun, J. T. Gaskins, F. Deangelis, A. Henry, and P. E. Hopkins, Interfacial defect vibrations enhance thermal transport in amorphous multilayers with ultrahigh thermal boundary conductance. Adv. Mater. **30**, 1804097 (2018).

[27] S. W. King, M. M. Paquette, J. W. Otto, A. N. Caruso, J. Brockman, J. Bielefeld, M. French, M. Kuhn, and B. French, Valence and conduction band offsets at amorphous hexagonal boron nitride interfaces with silicon network dielectrics, Appl. Phys. Lett. **104**, 102901 (2014).

[28] W. A. Lanford, M. Parenti, B. J. Nordell, M. M. Paquette, A. N. Caruso, M. Mäntymäki, J. Hämäläinen, M. Ritala, K. B. Klepper, V. Miikkulainen, O. Nilsen, W. Tenhaeff, N. Dudney, D. Koh, S. K. Banerjee, E. Mays, J. Bielefeld, and S. W. King, Nuclear reaction analysis for H, Li, Be, B, C, N, O and F with an RBS check, Nucl. Instrum. Methods Phys. Res. B **371**, 211 (2016).

[29] See Supplemental Material at http://link.aps.org/supplemental/10.1103/PhysRevMaterials.4.073603 for tables of sample properties, measurement and analysis details, additional TEM images, and the full elastic properties results on SiOC:H films.

[30] J. C. Phillips and M. F. Thorpe, Constraint theory, vector percolation and glass formation, Solid State Commun. **53**, 699 (1985).

[31] J. C. Mauro, Topological constraint theory of glass, Am. Ceram. Soc. Bull. **90**, 31 (2011).

[32] Q. Li, K. Hoogeboom-Pot, D. Nardi, M. M. Murnane, H. C. Kapteyn, M. E. Siemens, E. H. Anderson, O. Hellwig, E. Dobisz, B. Gurney, R. Yang, and K. A. Nelson, Generation and control of ultrashort-wavelength two-dimensional surface acoustic waves at nanoscale interfaces, Phys. Rev. B **85**, 195431 (2012).

[33] I. Horcas, R. Fernández, J. M. Gómez-Rodríguez, J. Colchero, J. Gómez-Herrero, and A. M. Baro, WSXM: A software for scanning probe microscopy and a tool for nanotechnology, Rev. Sci. Instrum. **78**, 013705 (2007).

[34] A. Rundquist, C. G. Durfee, Z. Chang, C. Herne, S. Backus, M. M. Murnane, and H. C. Kapteyn, Phase-matched generation of coherent soft X-rays, Science **280**, 1412 (1998).

[35] R. I. Tobey, M. E. Siemens, O. Cohen, M. M. Murnane, H. C. Kapteyn, and K. A. Nelson, Ultrafast extreme ultraviolet holography: Dynamic monitoring of surface deformation, Opt. Lett. **32**, 286 (2007).

[36] D. Nardi, F. Banfi, C. Giannetti, B. Revaz, G. Ferrini, and F. Parmigiani, Pseudosurface acoustic waves in hypersonic surface phononic crystals, Phys. Rev. B **80**, 104119 (2009).

[37] D. Nardi, M. Travagliati, M. E. Siemens, Q. Li, M. M. Murnane, H. C. Kapteyn, G. Ferrini, F. Parmigiani, and F. Banfi, Probing thermomechanics at the nanoscale: Impulsively excited pseudosurface acoustic waves in hypersonic phononic crystals. Nano Lett. **11**, 4126 (2011).

[38] COMSOL, Inc., COMSOL Multiphysics, Version 4.3b (COMSOL, Inc., 2013).

[39] L. Bluestein, A Linear Filtering Approach to the Computation of Discrete Fourier Transform, IEEE Trans. Audio Electroacoust. **18**, 451 (1970).

[40] J. Chen, E. Louis, C. J. Lee, H. Wormeester, R. Kunze, H. Schmidt, D. Schneider, R. Moors, W. Schaik, M. Lubomska, and F. Bijkerk, Detection and Characterization of Carbon Contamination on EUV Multilayer Mirrors, Opt. Express **17**, 16969 (2009).

[41] T. Denneulin, D. Cooper, J.-M. Hartmann, and J.-L. Rouviere, The addition of strain in uniaxially strained transistors by both SiN contact etch stop layers and recessed SiGe sources and drains, J. Appl. Phys. **112**, 094314 (2012).

[42] B. Abad Mayor, J. L. Knobloch, T. D. Frazer, J. N. Hernandez-Charpak, H. Y. Cheng, A. J. Grede, N. C. Giebink, T. E. Mallouk, P. Mahale, N. N. Nova, A. A. Tomaschke, V. L. Ferguson, V. H. Crespi, V. Gopalan, H. C. Kapteyn, J. V. Badding, and M. M. Murnane, Nondestructive measurements of the mechanical and structural properties of nanostructured metalattices, Nano Lett. **20**, 3306 (2020).

[43] J. L. Arlein, S. E. M. Palaich, B. C. Daly, P. Subramonium, and G. A. Antonelli, Optical pump-probe measurements of sound velocity and thermal conductivity of hydrogenated amorphous carbon films, J. Appl. Phys. **104**, 033508 (2008).

[44] H. T. Grahn, H. J. Maris, J. Tauc, and B. Abeles, Time-resolved study of vibrations of a-Ge:H/a-Si:H multilayers, Phys. Rev. B **38**, 6066 (1988).

[45] C. Rossignol, B. Perrin, B. Bonello, P. Djemia, P. Moch, and H. Hurdequint, Elastic properties of ultrathin permalloy/alumina multilayer films using picosecond ultrasonics and brillouin light scattering, Phys. Rev. B **70**, 094102 (2004).

[46] Y. Matsuda, S. W. King, J. Bielefeld, J. Xu, and R. H. Dauskardt, Fracture properties of hydrogenated amorphous silicon carbide thin films, Acta Mater. **60**, 682 (2012).

[47] Y. Matsuda, S. W. King, and R. H. Dauskardt, Tailored amorphous silicon carbide barrier dielectrics by nitrogen and oxygen doping, Thin Solid Films **531**, 552 (2013).